Nano Research

Open Access

Research Article

The mechanism of hierarchical regulation to improve stability of heavy-metal-free Zn:$CuFeS_2$ quantum dots sensitized solar PEC cells for highly-efficient hydrogen evolution

Yang Lian, Shuai Shao, Yunlong Du, Yunna Gao, Jinwen Yi, and Wei Zheng ✉

School of Material Science and Chemical Engineering, Harbin University of Science and Technology, Harbin 150040, China

Cite this article: *Nano Research*, **2026**, *19*, 94908672. https://doi.org/10.26599/NR.2026.94908672

ABSTRACT: The photo-corrosion of sulfide quantum dots (QDs) always limits the applications in photoelectrochemical (PEC) cells as photo-sensitizers. Herein, Zn-doped $CuFeS_2$ (ZCIS) QDs were synthesized to sensitize TiO_2/F-doped tin oxide (FTO) glass photoanode. After Zn introduction, the highly chemically active S_2^{2-} in $CuFeS_2$ (CIS) QDs disappears, and the average grain size of Zn:$CuFeS_2$ reduces, enhancing the quantum confinement effect that accelerates the separation and transfer of photogenerated carriers. After coated with ZnS passivation layer, ZnS/ZCIS/TiO_2/FTO photoanode was employed for H_2 evolution together with a Pt sheet electrode in aqueous electrolyte. The I-type ZnS/ZCIS heterojunction not only suppresses back electron transfer, but also promotes transfer of carriers furtherly. Zn doping and ZnS coating inhibit photo-corrosion of ZCIS QDs, and improve PEC performance and stability significantly. Under one sun illumination (100 mW/cm²), ZnS/ZCIS/TiO_2/FTO photoanode based cell has achieved accumulative H_2 yield of 642.17 μmol/cm² for 4 h with average rate of 160.54 μmol/(cm²·h) at 0.6 V bias. After 16-h H_2 evolution in 4-cycle test, the average rate decreases by only 2.13%.

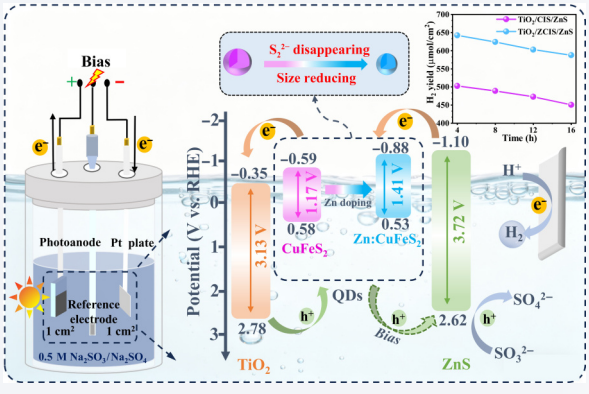

KEYWORDS: solar photoelectrochemical (PEC) cells, hydrogen evolution, photo-corrosion, sulfide quantum dots (QDs), stability

1 Introduction

The rapid consumption of global fossil fuels and the severe environmental problems have increased the demand for clean and sustainable energy significantly. Hydrogen energy is regarded as an ideal candidate contributing to the future sustainable energy system due to its high energy density and zero carbon emissions [1]. Inorganic semiconductor quantum dots (QDs) sensitized solar photoelectrochemical (PEC) cells have been applied for hydrogen evolution widely because of many advantages, such as high utilizing efficiency on solar spectrum, the low cost of materials preparation and device assembly, direct and efficient energy conversion, and stable device structure without secondary pollution [2, 3].

However, photo-corrosion phenomenon of sulfide QDs as the popular solar sensitizer triggers the instability of devices that limits their applications in solar PEC cells greatly [4, 5]. The photo-corrosion of sulfide QDs refers to the process in which, under light illumination, the photogenerated carriers undergo chemical reactions with the surrounding environment, leading to the destruction of the chemical composition and crystal structure of QDs, and ultimately resulting in the loss of their original optical and electrical properties [6]. For instance, the photo-generated holes (h^+) attack S^{2-} in the lattice preferentially, oxidizing it into elemental S or SO_4^{2-}, leading to sulfur loss or lattice collapse, rather than participating in the designed reaction, for example, water-splitting oxidation evolution reaction (OER) [7]. To address this challenge, researchers have proposed a variety of strategies to suppress the photo-corrosion of sulfide QDs to enhance their stability. The coating or passivation on QDs' surface is one of the most direct and effective methods. Kwon team designed AgInZnS/CdS/ZnS core–shell–shell structure QDs to passivate surface defects effectively and prevent direct contact of the electrolyte with QDs with ZnS layer in 2.9 nm thickness through atomic layer deposition (ALD) technology [8]. Cao group loaded

Received: November 1, 2025; **Revised:** March 2, 2026
Accepted: March 23, 2026

✉Address correspondence to zhengwei1972@sina.com

$ZnFe_2O_4$ nanoparticles as hole extraction and protective layer on CdS QDs/ZnO nanorods in core/shell structure to provide active sites for accelerating the consumption of holes in water-spitting OER oxidation rather than corrosion of QDs, and the initial photocurrent density remained at 85.1% after 1 h of illumination [9]. An internal electric field can accelerate charge separation through constructing heterojunction structures to inhibit photo-corrosion. Hu group induced the crystallization of CdS QDs on the surface of polyimide to form a direct Z type charge transfer channel, promoting the spatial separation of photogenerated carriers, and achieving continuous hydrogen production for 16 h with the increasing activity [10]. The photo-corrosion can be inhibited through regulating the microstructure or control the electronic structure and defect chemistry of QDs. Luo prepared the hollow spherical $Zn_{0.8}Cd_{0.2}S$ QDs to reduce the exposure of surface-active sites to sensitize the photoanode, and hydrogen yield decayed 14.5% after 4 cycles [11]. Nie adjusted the stoichiometric ratio of $CuInSe_2$ and doped it with Zn^{2+} to synthesize high-quality Zn:$CuInSe_2$/ZnS QDs in core–shell structure, exhibiting stable photoluminescence quantum yield (PLQY) of 62.7% at wavelength of 810 nm, which was attributed to the cation exchange between Zn^{2+} and Cu^{+} or In^{3+} to optimize the composition of QDs [12].

The I–III–VI $CuFeS_2$ (CIS) in chalcopyrite structure as one of Pt- and Cd-free QDs have attracted much attention due to their narrow band gap (E_g, about 1.0–1.5 eV), high light absorption coefficient, abundant crustal reserves of constitutive elements with low nuclear charge number ($Z < 30$), and tunable band structure [13, 14]. Herein, heavy-metal-free Zn:$CuFeS_2$ (ZCIS) QDs were designed through Zn doping in $CuFeS_2$ QDs to optimize the composition for enhancing light absorption and especially, decrease the formation of S_2^{2-} which is very active and can react with both oxidants and reductants. When chalcopyrite $CuFeS_2$ serves as an electrocatalyst, the generation of surface S–S bonded species (e.g., S_2^{2-}) is well established as one of the critical factors triggering stability deterioration [15, 16]. In addition to its intrinsic chemical evolution, this process is frequently accompanied by the disruption of metal ion valence states (e.g., Fe^{3+} reduction), where the concomitant charge transfer impairs the local lattice integrity [17], resulting in higher stability in PEC hydrogen evolution significantly. The prepared Zn:$CuFeS_2$ QDs in hot-injection process were loaded onto TiO_2 nanorod array films on F-doped tin oxide (FTO) glass substrate and then, ZnS QDs as the passivation layer were synthesized via *in-situ* successive ionic layer adsorption and reaction (SILAR) process to construct ZnS/Zn:$CuFeS_2$/TiO_2/FTO photoanode. Besides for decreasing the surface defects, the coating of ZnS forms I-type ZnS/Zn:$CuFeS_2$ heterojunction to suppress back electron transfer in photoanodes for improving PEC performance [18]. The substituting of Zn^{2+} ions in $CuFeS_2$ QDs and the introducing of ZnS passivation layer are the hierarchically-regulated and synergistic strategy to promote the stability of photoanodes and PEC performance of cells. Under one-sun illumination (AM 1.5G, 100 mW/cm^2) at bias of 0.6 V, hydrogen yield reached 642.16 μmol/cm^2 within 4 h with highly stable photocurrent density of ~ 6.8 mA/cm^2, and especially, hydrogen evolution rate maintained 91.48% after a cumulative 16-h hydrogen evolution cycle test, which also has taken the first place in heavy-metal-free QDs sensitized solar PEC cells for hydrogen evolution based on recent reports. The mechanism to improve the stability of heavy-metal-free Zn:$CuFeS_2$ QDs sensitized solar PEC cells for hydrogen evolution was investigated systematically, and the new details were proposed and verified experimentally, which must offer more ideas and experimental basis to solve the problem of sulfide QDs' photo corrosion in the PEC applications of solar cell devices.

2 Experimental

The details of CIS, ZCIS QDs, and photoanodes preparation, and characterizations and measurements of cell samples are recorded in the Electronic Supplementary Material (ESM). The whole preparation process of four photoanodes named as CIS/TiO_2, ZCIS/TiO_2, ZnS/CIS/TiO_2, and ZnS/ZCIS/TiO_2 has been illustrated in Fig. 1. The cell samples were assembled with prepared photoanodes and Pt sheet counter electrode in electrolyte of 0.5 M Na_2SO_3/Na_2SO_4 (or Na_2SO_4) solution with effective photoanode area 1.0 cm^2.

3 Results and discussion

3.1 Characterizations of QDs and photoanodes

CIS and ZCIS QDs have been characterized through electronic microscopy, X-ray diffraction (XRD), Raman spectroscopy, and X-ray photoelectron spectroscopy (XPS). As shown in Figs. 2(a)–2(c) for CIS and Figs. 2(d)–2(f) for ZCIS, the average size of spherical CIS and ZCIS QDs is 7.18 ± 0.2 and 5.82 ± 0.3 nm, respectively. This significant size reduction after Zn doping is primarily attributed to the substitution of Cu^{+} ions (ionic radius ~ 0.77 Å) by smaller Zn^{2+} ions (~ 0.74 Å) in the lattice, which induces a unit cell contraction. This lattice distortion increases the surface energy and alters the growth kinetics, leading to higher nucleation density and lower final growth limit under the identical synthetic conditions. In the high-resolution transmission electron microscopy (HRTEM) images (Figs. 2(b) and 2(e)), it can be observed that both CIS and ZCIS have clear lattice fringes with spacings of 0.304 and 0.305 nm which correspond to (112) crystal plane of chalcopyrite $CuFeS_2$ crystal, respectively. In addition, the diffraction rings appeared in the selected area electron diffraction (SAED) patterns of CIS and ZCIS (Figs. 2(c) and 2(f)) are both labeled as (101), (211), and (213) planes of chalcopyrite $CuFeS_2$, further confirming that the incorporation of Zn does not change the crystal phase with good crystallinity.

XRD patterns (Fig. 3(a)) verify the crystalline phase of CIS and ZCIS QDs which both are consistent with chalcopyrite $CuFeS_2$ (PDF#37-0471). Besides characteristic diffraction peaks corresponding to (112), (220), (204), (312), and (116) planes of $CuFeS_2$ crystals, a splitting peak at 27.86° near to (112) peak at

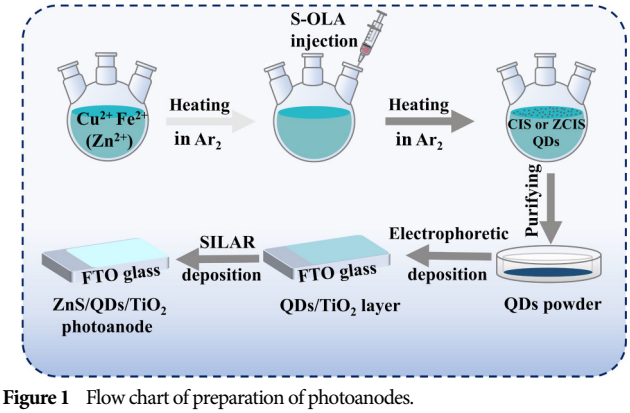

Figure 1 Flow chart of preparation of photoanodes.

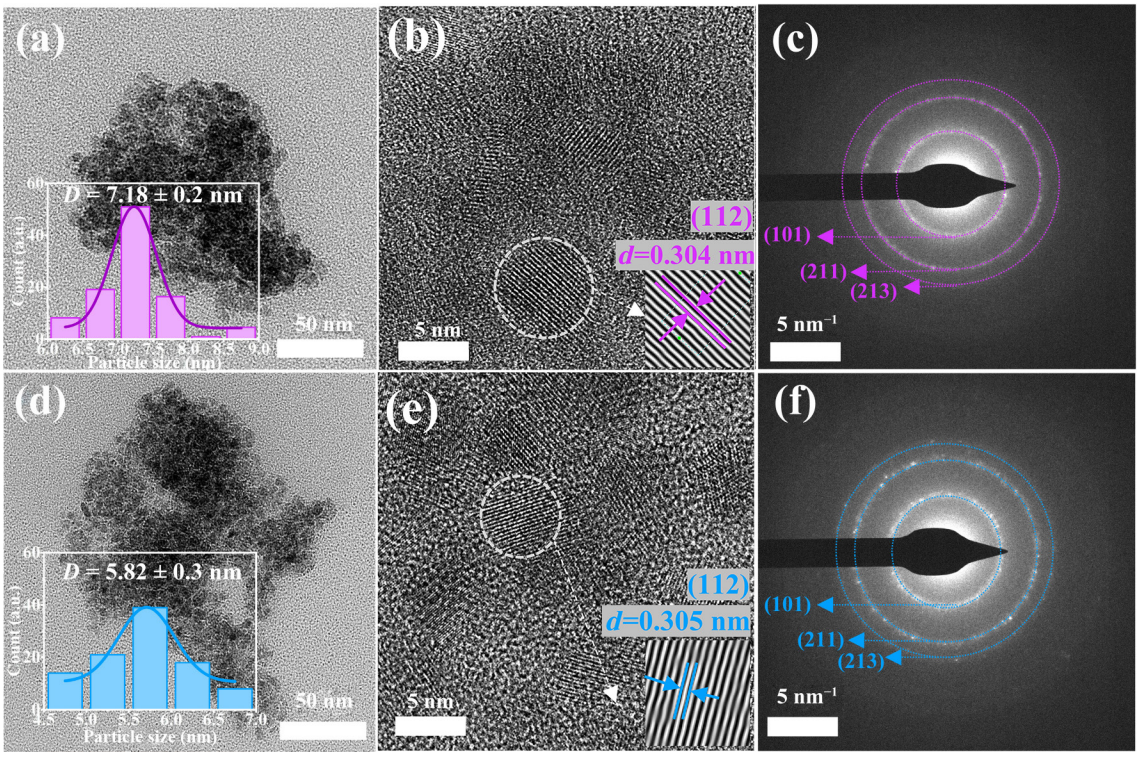

Figure 2 The characterization of two QDs. (a) TEM image, (b) HRTEM image, and (c) SAED pattern of CIS QDs. (d) TEM image, (e) HRTEM image, and (f) SAED pattern of ZCIS QDs.

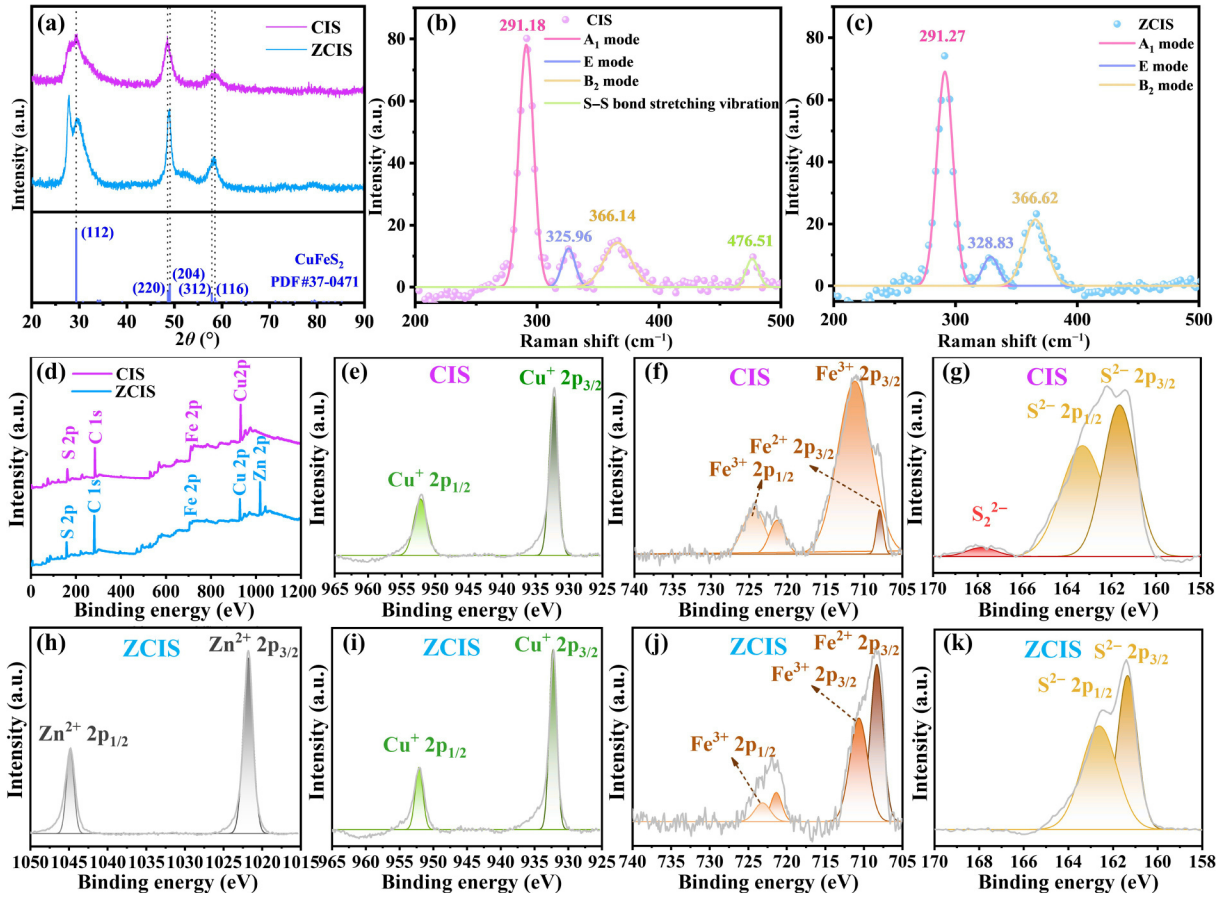

Figure 3 Defect characterizations of two QDs. (a) XRD patterns. Raman spectra of (b) CIS and (c) ZCIS QDs. (d) XPS survey spectra and high-resolution XPS spectra of ((e)–(g)) CIS and ((h)–(k)) ZCIS QDs.

29.32° comes from CuS (PDF#78-2121) impurity in both CIS and ZCIS. After Zn doping, all characteristic diffraction peaks of $CuFeS_2$ shift rightwards a little (0.1°–0.2°), and detail data are recorded in Table S1 in the ESM, which represents the contraction of unit cells [19]. Since the electronegativity of Zn^{2+} is larger than that of Cu^+, while smaller than that of Fe^{3+}, it is deduced that Zn replaces Cu, which is also be proved with relative intensity change of CuS diffraction peak at 27.86°. If Zn occupies Cu site, the replaced Cu will react with S, leading to the intensity increase of diffraction peak CuS.

Raman spectra in Figs. 3(b) and 3(c) clearly reveal the effect of Zn doping on the structure of QDs. The distinct peak at 476.51 cm^{-1} in CIS QDs corresponds to the characteristic stretching vibration of S–S bond in S_2^{2-}, verifying the existence of S_2^{2-} defects in CIS QDs. This peak completely disappears in ZCIS QDs after Zn doping. Meanwhile, the main lattice vibration modes show systematic blue-shift. The strongest A_1 mode peak shifts from 291.18 to 291.27 cm^{-1}, E mode peak from 325.96 to 328.83 cm^{-1} and B_2 mode peak from 366.14 to 366.62 cm^{-1}. This overall blue-shift is mainly attributed to the quantum confinement effect induced by the reduced QD size (from 7.18 to 5.82 nm), which constrains the bond vibrations, thereby increasing the energy required for vibration.

XPS spectra of CIS and ZCIS in Fig. 3(d) exhibit characteristic peaks of S, Fe, Cu, and Zn elements, and verify Zn incorporation. It is determined that Zn occupies Cu site in ZCIS due to the obvious decrease of Cu atomic percentage through comparing elemental atomic contents between and CIS and ZCIS that are listed in Table S2 in the ESM. By comparing the high-resolution XPS spectra of CIS (Figs. 3(e)–3(g)) and those of ZCIS (Figs. 3(h)–3(k)), it is concluded that Zn doping does not change the crystal phase structure and Zn^{2+} substitutes intrinsic Cu^+, which was consistent with the results of XRD, transmission electron microscopy (TEM), HRTEM, and Raman. What should be emphasized is that increase of Fe^{2+} (comparing Fig. 3(f) with Fig. 3(j)) and especially disappearance of S_2^{2-} (comparing Fig. 3(g) with Fig. 3(k)) after Zn doping. This conclusion agrees well with the result of Raman spectra. There are two kind of defects $(Fe^{2+}_{Fe3+})^-$ and $(S_2^{2-}{}_{S2-})^-$ in CIS. Zn^{2+} substitutes intrinsic Cu^+, forming positive defects $(Zn^{2+}_{Cu+})^+$, and therefore, increase of $(Fe^{2+}_{Fe3+})^-$ and disappearance of $(S_2^{2-}{}_{S2-})^-$ can maintain electrical neutrality of ZCIS [20]. Based on above-mentioned photo-corrosion principle of sulfide QDs, disappearance of S_2^{2-} is helpful to improve the stability of sulfide QDs in PEC process due to the high chemical activity of S_2^{2-} with both reducing and oxidizing abilities.

CIS or ZCIS QDs were deposited on TiO_2 nanorod arrays on FTO glass, and then ZnS layer was coated on it to prepare ZnS/CIS/TiO_2 or ZnS/ZCIS/TiO_2 photoanode. Figure 4(a) shows XRD patterns of two photoanodes, and besides the characteristic diffraction peaks from SnO_2 (PDF#46-1088) and TiO_2 crystals (PDF#21-1276), diffraction peaks corresponding to (112), (220), and (204) planes of chalcopyrite $CuFeS_2$ (PDF#37-0471), and (200), (222), and (400) planes of sphalerite ZnS (PDF#05-0566) appear for both two photoanodes. The powder samples employed for TEM and HRTEM images of ZnS/CIS/TiO_2 (Figs. 4(b)–4(e)) and ZnS/ZCIS/TiO_2 (Figs. 4(f)–4(i)) photoanodes were scraped from the prepared photoanodes. CIS QDs and ZnS nanoparticles adhere to single crystalline TiO_2 rod, exhibiting lattice fringes with spacing of 0.349, 0.304, and 0.191 nm corresponding to (101), (112), and (220) planes of TiO_2, $CuFeS_2$, and ZnS crystal, respectively. In ZnS/ZCIS/TiO_2, ZCIS QDs and ZnS nanoparticles also adhere to single crystalline TiO_2 rod, identifying lattice fringes with spacings of 0.189, 0.187, and 0.163 nm corresponding to (200), (220), and (311) planes of TiO_2, $CuFeS_2$, and ZnS crystal, respectively. The cross-sectional scanning electron microscopy (SEM) images (Fig. S1 in the ESM) reveal that the ZnS layer deposited via the SILAR method forms a conformal nanoscale coating on the ZCIS/TiO_2 photoanode rather than continuous thick film. Consequently, it is challenging to visually distinguish the ZnS nanoparticles from the underlying ZCIS QDs. Therefore, energy-dispersive X-ray spectroscopy (EDS) was employed to perform elemental analysis and verify the elemental composition. Figures S2 and S3 in the ESM record the results of EDS point and mapping analysis of ZnS/CIS/TiO_2 and ZnS/ZCIS/TiO_2, respectively. The characteristic peaks of Ti, O, Fe, S, Cu, and Zn elements are all displayed in EDS spectra clearly, and quantitative analysis of elemental contents is inaccurate due to the existence of Cu mesh [21]. O, Zn, Fe, Cu, and S in ZnS/CIS/TiO_2 and ZnS/ZCIS/TiO_2 present highly uniform and continuous distribution, and however, Ti mapping exhibits rod shape, which is consistent with SEM images of TiO_2 rod arrays in

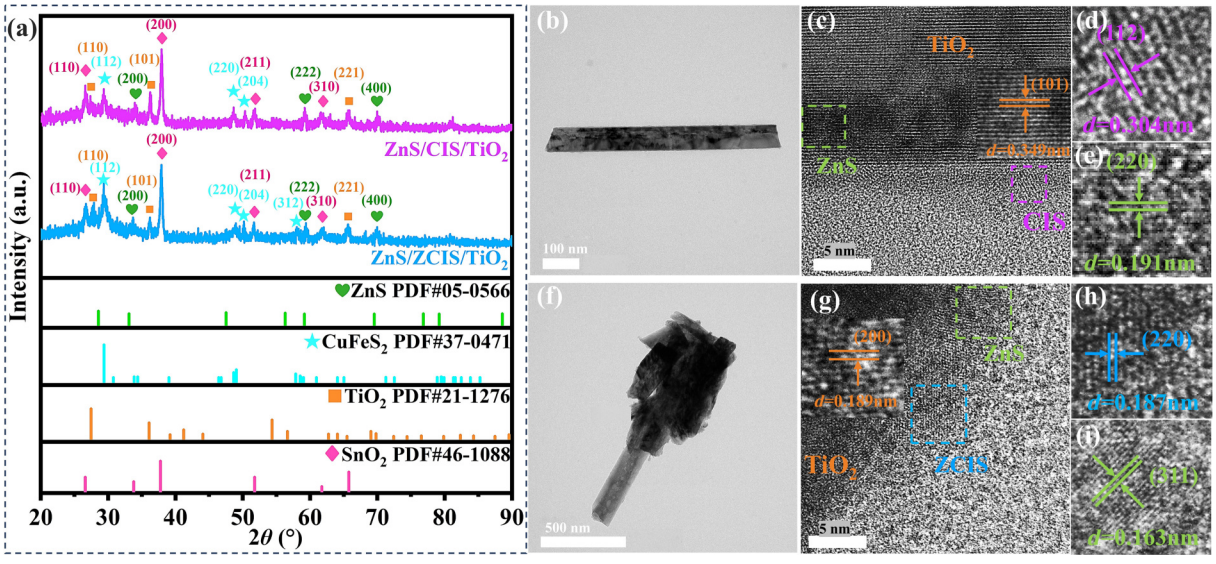

Figure 4 The characterization of two photoanodes. (a) XRD patterns. TEM and HRTEM images for ((b)–(e)) ZnS/CIS/TiO_2 and ((f)–(i)) ZnS/ZCIS/TiO_2 photoanodes.

Fig. S4 in the ESM. This facilitates the deposition of QDs and rapid transport of photogenerated carriers in PEC process.

Ultraviolet–visible (UV–Vis) spectra and corresponding Tauc plots of CIS and ZCIS QDs are shown in Figs. 5(a) and 5(b), while those of TiO_2 are presented in Figs. S5(a) and S5(b) in the ESM. Notably, TiO_2 exhibited strong absorption only in the ultraviolet region [22], whereas CIS and ZCIS QDs significantly extended the light absorption range into the visible region. Based on Eq. (S1) in the ESM, the E_g of CIS, ZCIS, and TiO_2 was calculated from the Tauc plots to be 1.17, 1.41, and 3.13 eV, respectively. It is noteworthy that E_g of ZCIS is larger than that of CIS, which can be attributed to the Burstein–Moss effect [23]. The substitution of Cu^+ by Zn^{2+} results in the shift the Fermi level into valence band (VB) of ZCIS, leading to an increase of E_g. Density functional theory (DFT) calculations were performed to examine the modifications in the electronic band structure of $CuFeS_2$ induced by Zn doping and to corroborate the experimentally observed increase in E_g. The fundamental electronic structure of chalcopyrite $CuFeS_2$ is depicted in Fig. S6(a) in the ESM. Employing a unit cell composed of 4 Cu, 4 Fe, and 8 S atoms, and incorporating spin polarization effects of the d-orbitals, the resulting band structure and density of states (Figs. S6(b) and S6(c) in the ESM) reveal a calculated direct bandgap of 0.77 eV for CIS. For ZCIS, modeled using a unit cell containing 2 Cu, 2 Zn, 4 Fe, and 8 S atoms, the electronic structure is presented in Fig. S6(d) in the ESM. The corresponding band structure and density of states (Figs. S6(e) and S6(f) in the ESM) demonstrate an increased bandgap of 0.98 eV. Although this observed trend aligns well with optical measurement data, the integrated analysis of bulk DFT simulations does not consider quantum confinement, alongside experimental results, confirming that Zn doping effectively enlarges E_g of $CuFeS_2$. This bandgap modulation is advantageous for applications necessitating precise band alignment, including photovoltaic and photocatalytic technologies. The marginally lower bandgap values derived from DFT relative to experimental findings are ascribed to quantum confinement effects.

The valence band maximum (VBM) positions of CIS and ZCIS QDs were determined through ultraviolet photoelectron spectroscopy (UPS) measurements. Analysis of the UPS and high-resolution UPS (HRUPS) spectra shown in Figs. 5(c)–5(e) revealed the photoelectron cut-off energies ($E_{cut\text{-}off}$) of 16.98 and 17.06 eV for CIS and ZCIS QDs, respectively. The valence band onset energies (E_{onset}), derived from HRUPS data in Fig. 5(e), were measured at 1.19 eV for CIS and 1.22 eV for ZCIS. Utilizing Eq. (S2) in the ESM, the corresponding VBM positions were calculated as 0.58 and 0.53 V vs. reversible hydrogen electrode (RHE) for CIS and ZCIS, respectively. Combined with the above-mentioned bandgaps from UV–Vis spectra, the conduction band minimum (CBM) levels were subsequently determined to be −0.59 V for CIS and −0.88 V for ZCIS. The flat-band potential (P_{fb}) of TiO_2 was calculated from the Mott–Schottky plot of Fig. S5(c) in the ESM. CBM of TiO_2 as

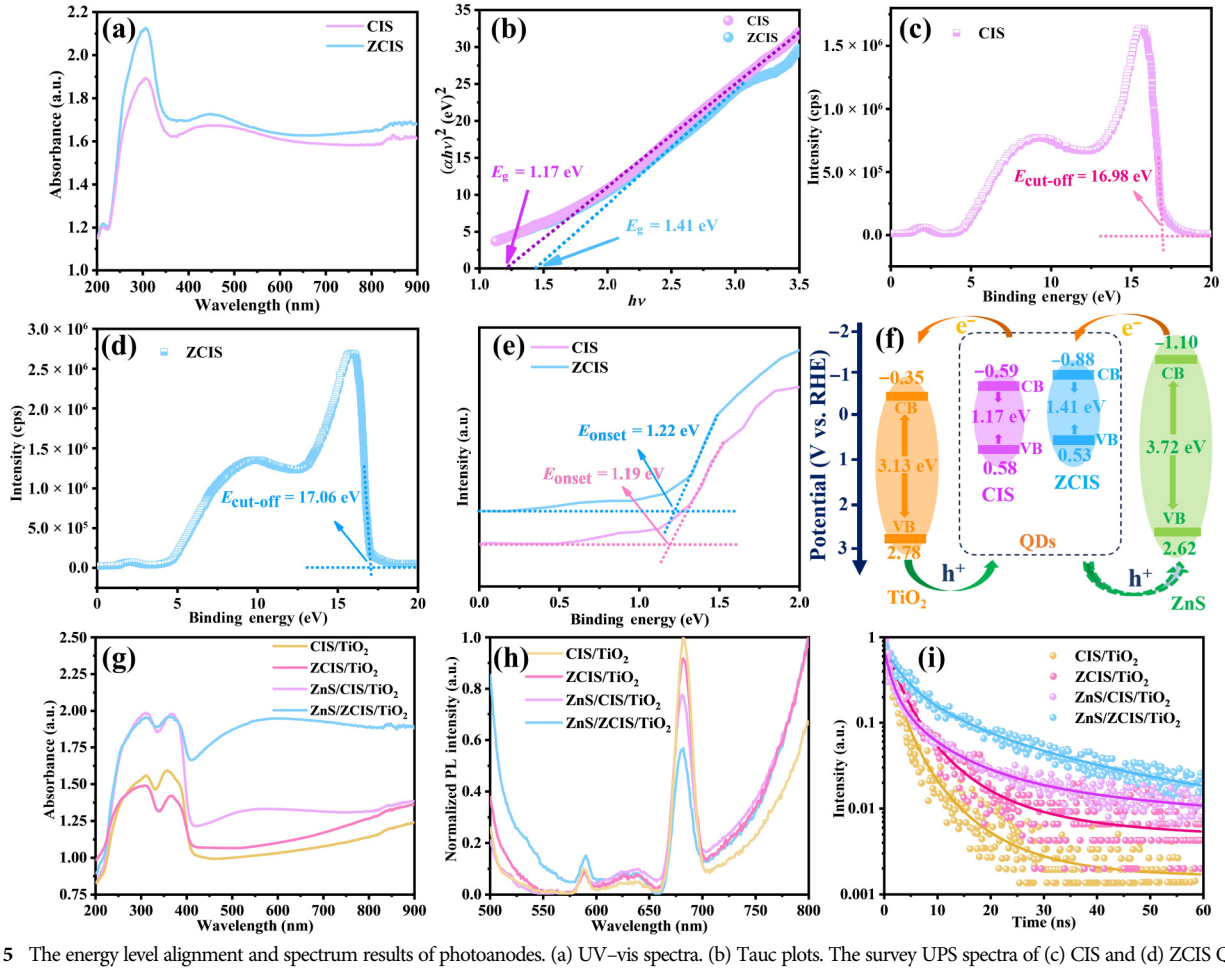

Figure 5 The energy level alignment and spectrum results of photoanodes. (a) UV–vis spectra. (b) Tauc plots. The survey UPS spectra of (c) CIS and (d) ZCIS QDs. (e) High-resolution UPS spectra of CIS and ZCIS QDs. (f) The obtained band structure diagram of photoanodes. (g) UV–vis spectra. (h) Steady-state PL spectra and (i) time-resolved PL decay curves of different photoanodes.

an n-type semiconductor is typically positioned approximately 0.2 V more negative than P_{fb} [24, 25]. Therefore, CBM and VBM of TiO_2 is determined to be −0.35 and 2.78 V vs. RHE, respectively. Band alignment data for ZnS can be sourced from prior studies, which is utilized in the present work involving the *in-situ* SILAR technique for the deposition of the ZnS layer [26]. Consequently, the energy band alignment for CIS and ZCIS QDs sensitized photoanodes was collectively illustrated in Fig. 5(f). Both CIS and ZCIS QDs form type-II heterojunctions with TiO_2, which facilitates the injection of photogenerated electrons into conduction band (CB) of TiO_2. Notably, Zn doping induces an overall upward shift in the energy band structure, thereby significantly enhancing the driving force for electron injection into TiO_2. Furthermore, CBM of ZCIS (−0.88 V) is more positive than that of ZnS (−1.10 V), effectively inhibiting back electron transfer from ZCIS to the ZnS layer and interfacial recombination. The transfer of holes from VB of TiO_2 (2.78 V vs. RHE) to that of ZCIS (0.53 V vs. RHE) proceeds spontaneously. However, the potential barrier exists for hole transfer from VB of ZCIS (0.53 V vs. RHE) to VB of ZnS (2.62 V vs. RHE). To overcome this barrier, an applied bias of 0.6 V vs. RHE is necessary, serving as the primary driving force that facilitates the transfer of holes to photoanode/electrolyte interface, thereby enabling the oxidation reaction. In addition, given the discrepancy between the potential barrier (~ 1.7 eV) and applied bias (0.6 V vs. RHE) as well as the nanoscale thickness of the ZnS coating shown in Fig. S1 in the ESM, it is posited that quantum tunneling also contributes to hole transmission across the barrier in addition to the applied bias.

After the passivation of ZnS layer, light absorption of composite photoanodes is enhanced in the visible–near-infrared range as shown in Fig. 5(g). ZnS/ZCIS/TiO_2 photoanode shows higher absorption intensity compared to ZnS/CIS/TiO_2 photoanode, which is attributed to narrow bandgap of smaller ZCIS QDs and larger number of light absorption active sites due to higher specific surface area. As shown by the normalized photoluminescence (PL) spectra in Fig. 5(h), ZCIS/TiO_2 exhibits lower fluorescence intensity compared to CIS/TiO_2, which is attributed to the more negative CB of ZCIS, thereby enhancing the driving force for electron transfer, and facilitating photogenerated electron–hole separation in type-II ZCIS/TiO_2 heterojunction. After the formation of another heterojunction ZCIS or CIS/ZnS, the fluorescence intensity is further reduced. ZnS/ZCIS/TiO_2 possesses the lowest fluorescence intensity, indicating the lowest carrier recombination efficiency. To investigate the charge carrier dynamics in photoanodes, the transient PL decay curves based on different photoanodes were recorded, as shown in Fig. 5(i). Through fitting the curves with the tri-exponential function in Eq. (S3) in the ESM, the average carrier lifetime (τ_{av}) and the goodness of fit were obtained and are summarized in Table S3 in the ESM. Compared to CIS/TiO_2 (179.58 ns), τ_{av} of ZCIS/TiO_2 extended to 218.91 ns. This enhancement is attributed to Zn doping, which optimizes the band alignment and reduces the interfacial charge transfer barrier between QDs and TiO_2. Furthermore, the introduction of ZnS passivation layer prolonged τ_{av} significantly, reaching 459.59 ns for ZnS/CIS/TiO_2 and 615.94 ns for ZnS/ZCIS/TiO_2. This pronounced improvement is primarily attributed to the electron-blocking function of the ZnS layer. The CBM of ZCIS (−0.88 V vs. RHE) is positioned more positively than that of ZnS (−1.10 V vs. RHE). This favorable energy offset creates an energetic barrier that effectively suppresses the back transfer of photo-generated electrons from ZCIS to the ZnS/electrolyte interface, thereby minimizing interfacial charge recombination and leading to the observed extension of carrier lifetime. Integrating these findings with UV–visible spectroscopy, band structure analyses, and PL spectral data, it is inferred that Zn doping not only enhances light absorption but also effectively inhibits electron–hole recombination, both of which are critical factors for the enhancement of PEC performance.

3.2 PEC performance for hydrogen evolution

Figure 6 evaluates PEC performance of different photoanodes systematically. As shown in Fig. 6(a), all PEC tests were conducted in standard three-electrode system constituting photoanodes, Pt plate counter electrode, and Ag/AgCl reference electrode in 0.5 M Na_2SO_4 aqueous solution electrolyte under one sun (AM 1.5G, 100 mW/cm^2), and all applied potentials were converted to RHE scale with Eq. (S4) in the ESM. The linear sweep voltammetry (LSV) curves in light illumination (Fig. 6(b)) prove that ZnS/ZCIS/TiO_2 based cell exhibits the largest photocurrent density, caused from the largest light absorption and the smallest fluoresce intensity among four samples. With the increase of applied voltage, photocurrent densities of all samples increase, which implies the definite electrocatalytic ability of cells. LSV curves in the dark (Fig. S7(a) in the ESM) show the current density variation expectedly. By comparing the current density (0.61 mA/cm^2) in the dark with photocurrent density (10.08 mA/cm^2) in the light both of ZnS/ZCIS/TiO_2 based cell at 1.23 V (vs. RHE), it is confirmed that the designed cell devices are suitable for solar PEC applications.

The applied bias photon-to-current efficiency (ABPE), calculated with Eq. (S5) in the ESM in Fig. 6(c) also shows the highest ABPE 3.13% of ZnS/ZCIS/TiO_2 photoanode, and in contrast 1.18% at the same voltage in the dark (Fig. S7(b) in the ESM). Notably, multiple ABPE peaks of all samples are supposed from the coexistence of multiple charge transfer pathways within composite photoanodes, which further validates the successful heterostructure construction of photoanodes. According to ABPE results of all samples, 0.6 V bias is adopted in the following PEC hydrogen evolution test based on the efficient utilization on electric and optical energy. Nyquist plots (Fig. 6(d)) from electrochemical impedance spectra (EIS) were employed to investigate charge transfer at photoanode/electrolyte interface, and the equivalent circuit was inserted, including series resistance (R_s), the charge transfer resistance (R_{ct}), counter electrode/electrolyte resistance (R_c), the capacitance (C), and constant phase element (Q_{CPE}). R_{ct}, R_s derived from fitting, and the goodness-of-fit (R^2) are documented in Table S4 in the ESM, with all R^2 values above 0.99, confirming excellent fitting reliability. Specifically, ZnS/ZCIS/TiO_2 photoanode presents a minimal R_{ct} of 8.71 kΩ/cm^2, reflecting the lowest barrier for photogenerated carrier transport across the photoanode–electrolyte interface.

Carrier transport and transfer dynamics were analyzed quantitively through calculating bulk separation efficiency (η_{bulk}) and surface injection efficiency ($\eta_{surface}$) of carriers based on Eqs. (S6)–(S9) in the ESM. η_{bulk} represents the efficiency of hole–electron separation in the photoanode, while $\eta_{surface}$ the injection efficiency of holes that reach photoanode surface to participate in reactions in electrolytes. Based on AM 1.5G standard solar spectrum (Fig. S8(a) in the ESM), light-harvesting efficiency (LHE, Fig. S8(b) in the ESM), and photocurrent density flux (Fig. S8(c) in the ESM), the absorbed photon flux (J_{abs}, Fig. S8(d) in the ESM) curves were derived. J_{abs} for CIS/TiO_2, ZCIS/TiO_2, ZnS/CIS/TiO_2, and

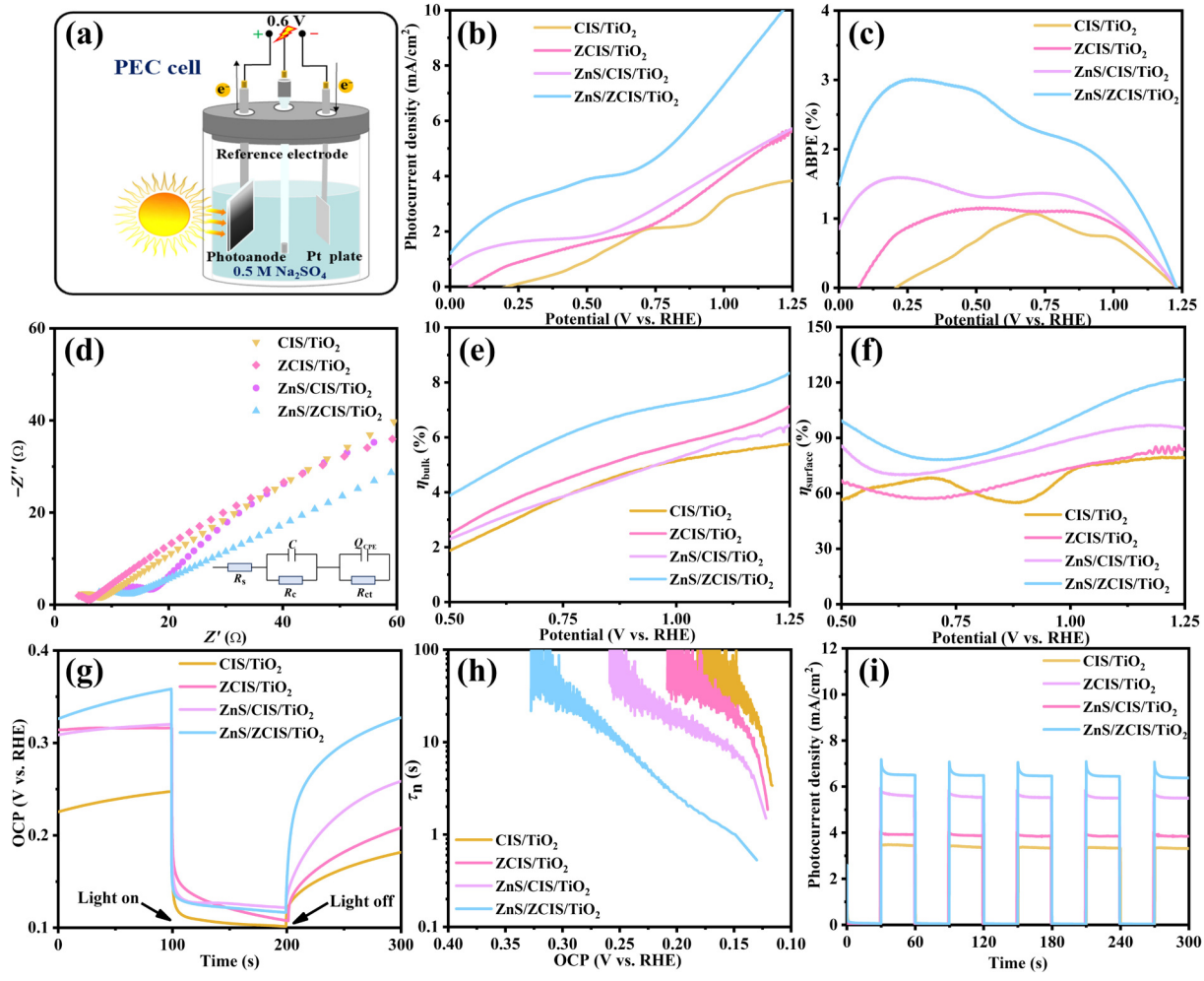

Figure 6 (a) Schematic for PEC cell structure, (b) LSV and (c) ABPE curves under illumination, (d) EIS Nyquist plots, (e) η_{bulk} curves, (f) $\eta_{surface}$ curves, (g) transient OCP, (h) potential-dependent carrier lifetime, and (i) transient *I*–*t* curves for different photoanodes in 0.5 M Na_2SO_4 aqueous solution.

$ZnS/ZCIS/TiO_2$ photoanodes at different absorption edges are listed in Table S5 in the ESM. Combined with LSV curves (Fig. S9 in the ESM) measured in 0.5 M Na_2SO_3/Na_2SO_4 electrolytes in the presence of hole scavenger SO_3^{2-}, η_{bulk} and $\eta_{surface}$ curves are shown in Figs. 6(e) and 6(f). $ZnS/ZCIS/TiO_2$ achieves exceptional η_{bulk} (8.18%) and $\eta_{surface}$ (121.23%) at 1.23 V (vs. RHE), obviously surpassing those of $ZnS/CIS/TiO_2$ (6.33% and 96.03%), $ZCIS/TiO_2$ (6.95% and 83.30%), and CIS/TiO_2 (5.72% and 79.23%). The transient open circuit potential (OCP) curves (Fig. 6(g)) were plotted to investigate carrier transport behavior in photoanodes at the existence of heterojunctions [27, 28]. Usually, larger OCP difference (V_{oc}) between the light and the dark, stronger migration ability of carriers in photoanodes. V_{oc} of CIS/TiO_2 and $ZCIS/TiO_2$ is 0.15 and 0.21 V, respectively, which is attributed to easier carrier transfer on heterojunction interface after Zn doping. After ZnS passivation layer coating, V_{oc} of $ZnS/CIS/TiO_2$ and $ZnS/ZCIS/TiO_2$ increases to 0.20 and 0.25 V, respectively, indicating that another heterojunction introduction accelerates carrier separation and transfer furtherly. The OCP-dependent carrier lifetime (τ_n) can be evaluated with OCP decay curve in Eq. (S10) in the ESM through fitting with exponential function (Fig. 6(h)) [29, 30]. A shorter τ_n generally indicates more efficient carrier separation and charge transfer in photoanodes. τ_n of CIS/TiO_2, $ZCIS/TiO_2$, $ZnS/CIS/TiO_2$, and $ZnS/ZCIS/TiO_2$ decreases as 3.39, 1.87, 1.51, and 0.53 s orderly, indicating after Zn doping and ZnS passivation layer coating, photoelectric conversion in $ZnS/ZCIS/TiO_2$ photoanode is the most efficient, so the bias has the smallest influence on the whole photoelectric process driven by solar light within four samples. The transient photocurrent density–time (*I*–*t*) curves (Fig. 6(i)) under one sun illumination at 0.6 V reveals that $ZnS/ZCIS/TiO_2$ based cell achieves the highest stable photocurrent density 6.8 ± 0.3 mA/cm² among four samples, which is consistent with the above results, including the largest light absorption, ABPE, carrier separation and injection efficiency, and the smallest resistance at photoanode/electrolyte interface.

$ZnS/ZCIS/TiO_2$ and $ZnS/CIS/TiO_2$ based PEC cells are employed for hydrogen evolution for 4 h under one sun illumination at 0.6 V (vs. RHE), and the results are shown in Fig. 7(a). $ZnS/ZCIS/TiO_2$ photoanode demonstrated higher cumulative hydrogen yield after 4 h, 642.17 μmol/cm² with average rate 160.54 μmol/(cm²·h), compared to 502.57 μmol/cm² and 125.64 μmol/(cm²·h) of $ZnS/CIS/TiO_2$ photoanode. All detail data are listed in Table S6 in the ESM. As shown in Fig. 7(b) of *I*–*t* curves within 4 h, the photocurrent density of $ZnS/CIS/TiO_2$ photoanode gradually decreased from about 10 mA/cm² at the beginning to 7.78 mA/cm² at the end, indicating significant degradation of PEC activity in spite of stable hydrogen evolution rate for 4 h, while the photocurrent density of $ZnS/ZCIS/TiO_2$ kept stable, maintaining at 10.89 ± 0.1 mA/cm² with negligible decay after 4 h.

The cyclic voltammetry (CV) curves scanned in 8 cycles within

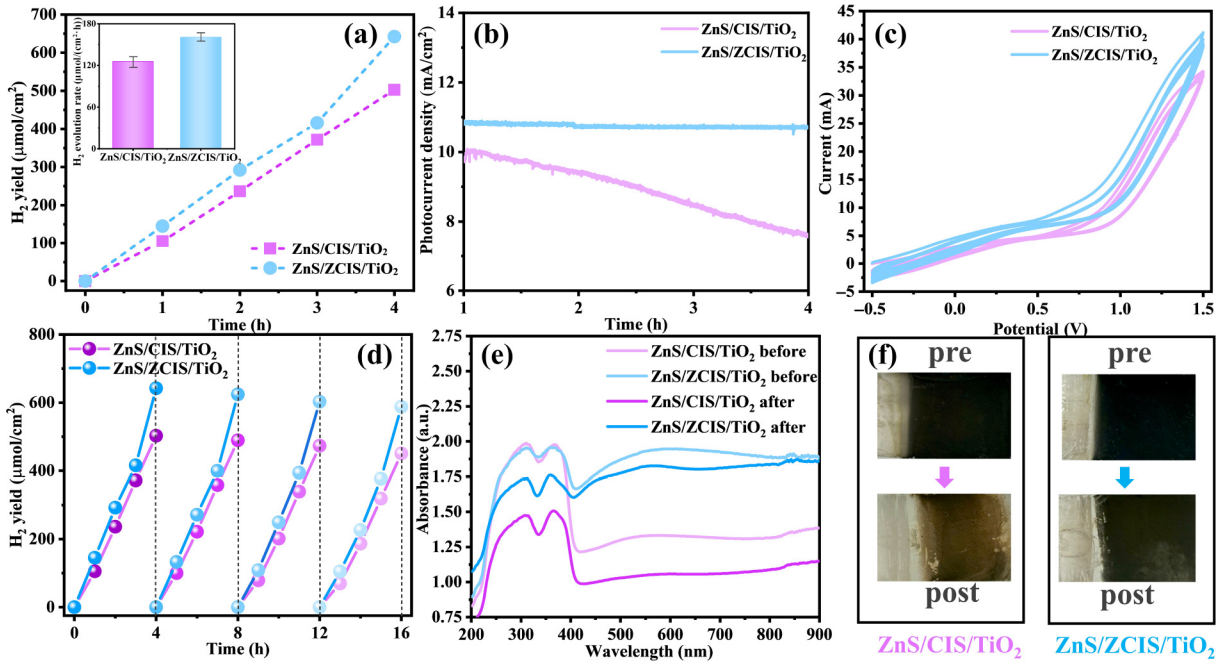

Figure 7 (a) H_2 yield and average rate within 4 h, (b) *I*–*t* curves, (c) CV curves, (d) H_2 yield curves, (e) UV–Vis spectra, and (f) the photo comparison before and after 16-h H_2 evolution within 4 cycles for ZnS/CIS/TiO_2 and ZnS/ZCIS/TiO_2 photoanodes.

−0.5 to 1.5 V (vs. RHE) shown in Fig. 7(c) illustrated highly overlapping feature for both two photoanodes, but as shown in Table S7 in the ESM, the effective area of the ZnS/ZCIS/TiO_2 photoanode decreased by only 1.67%, compared to 2.63% of ZnS/CIS/TiO_2 after 8 cycles, which also indicates higher PEC stability of ZnS/ZCIS/TiO_2 photoanode. Moreover, the area enclosed by CV curve of ZnS/ZCIS/TiO_2 was significantly larger than that of ZnS/CIS/TiO_2, reflecting the larger electrochemical surface area (ECSA). To further investigate the hydrogen evolution stability in longer period of two devices, 16-h hydrogen evolution test with 4 cycles are conducted for two devices. By comparing the results of Fig. 7(d), it is found that H_2 yield of ZnS/CIS/TiO_2 photoanode decreased by 10.47% after 16 h, while the yield of ZnS/ZCIS/TiO_2 photoanode decrease by only 8.52%, which indicates ZnS/ZCIS/TiO_2 photoanode demonstrates more excellent cycling durability in hydrogen evolution process. By comparing UV–Vis spectra before and after 16-h hydrogen evolution in Fig. 7(e), it was found that ZnS/ZCIS/TiO_2 photoanode retained most of its visible-light absorption, while ZnS/CIS/TiO_2 suffered relatively larger decrease. SEM images of Fig. S10 in the ESM for ZnS/CIS/TiO_2 and ZnS/ZCIS/TiO_2 photoanodes before and after 16-h hydrogen evolution reveal that the overall architecture of two photoanodes maintains structural integrity with negligible morphological alterations. Finally, in Fig. 7(f), the photos of two photoanodes before and after 16-h hydrogen evolution are compared to observe macroscopic change. ZnS/ZCIS/TiO_2 photoanode maintains its overall structural integrity with no obvious color change after 16-h test, indicating superior resistance to photo-corrosion and extremely strong structural stability compared to ZnS/CIS/TiO_2 photoanode.

3.3 Mechanism of stability improvement

To inhibit photo-corrosion of sulfide QDs sensitizer that impairs PEC H_2 yield and stability of solar cells, Zn elements were introduced into CIS QDs to form ZCIS, occupying intrinsic Cu^+ site as positive defect $(Zn^{2+}_{Cu+})^+$ which caused the disappearance of chemically active S_2^{2-}, as shown in Fig. 8(a). S_2^{2-} in CIS acts as negative defect $(S_2^{2-}{}_{S2-})^-$ and would be removed due to the existence of positive defect $(Zn^{2+}_{Cu+})^+$ after Zn doping. Meanwhile, Zn doping leads to lattice contraction and size reduction of QDs, widening the bandgap, which causes the enhance of so-called the quantum confinement effect [31, 32], as shown Fig. 8(b). The increased electric driving force accelerates the separation of photogenerated excitons and also inhibits electron–hole recombination in QDs due to smaller space. The faster exciton separation and carrier transfer outside QDs improve the photocurrent and also avoid the reaction between h^+ and S^{2-}, i.e., photo corrosion of sulfides.

The surface defects of QDs will trap the carriers to impair the photocurrent formation and therefore, ZnS passivation layer was deposited on QDs-sensitized photoanode to form the I-type heterojunction as shown in Fig. 8(c). ZnS layer functions as an electron blocking layer to suppress back electron transfer and interfacial recombination [33], since CB of ZnS is higher than that of ZCIS, and ZnS coating reduces the surface defect for higher photocurrent. Furthermore, since the initially synthesized CIS or ZCIS QDs are capped with organic ligands [34, 35], the application of ZnS coating effectively alters the surface properties of the photoanodes. Specifically, the ZnS layer converts the hydrophobic nature of CIS/TiO_2 (contact angle: 135.1°) and ZCIS/TiO_2 (134.5°) photoanodes into the hydrophilic state, as evidenced by the reduced contact angles of ZnS/CIS/TiO_2 (49.5°) and ZnS/ZCIS/TiO_2 (48.8°) in aqueous Na_2SO_3/Na_2SO_4 electrolyte, as illustrated in Fig. S11 in the ESM. Therefore, this modification in surface wettability is highly beneficial for PEC hydrogen evolution of the cell. Figure 8(d) illustrates the work principle of ZnS/ZCIS/TiO_2 photoanode|| Na_2SO_3/Na_2SO_4 electrolyte||Pt sheet cell under illumination at bias where h^+ oxidizes SO_3^{2-} to SO_4^{2-} on ZnS/ZCIS/TiO_2 photoanode, while e^- reduces H^+ to produce H_2, as shown in the inserted front-view and side-view photos of Pt sheet electrode in reacting process. As shown in Fig. 8(e) of photoanode energy band alignment,

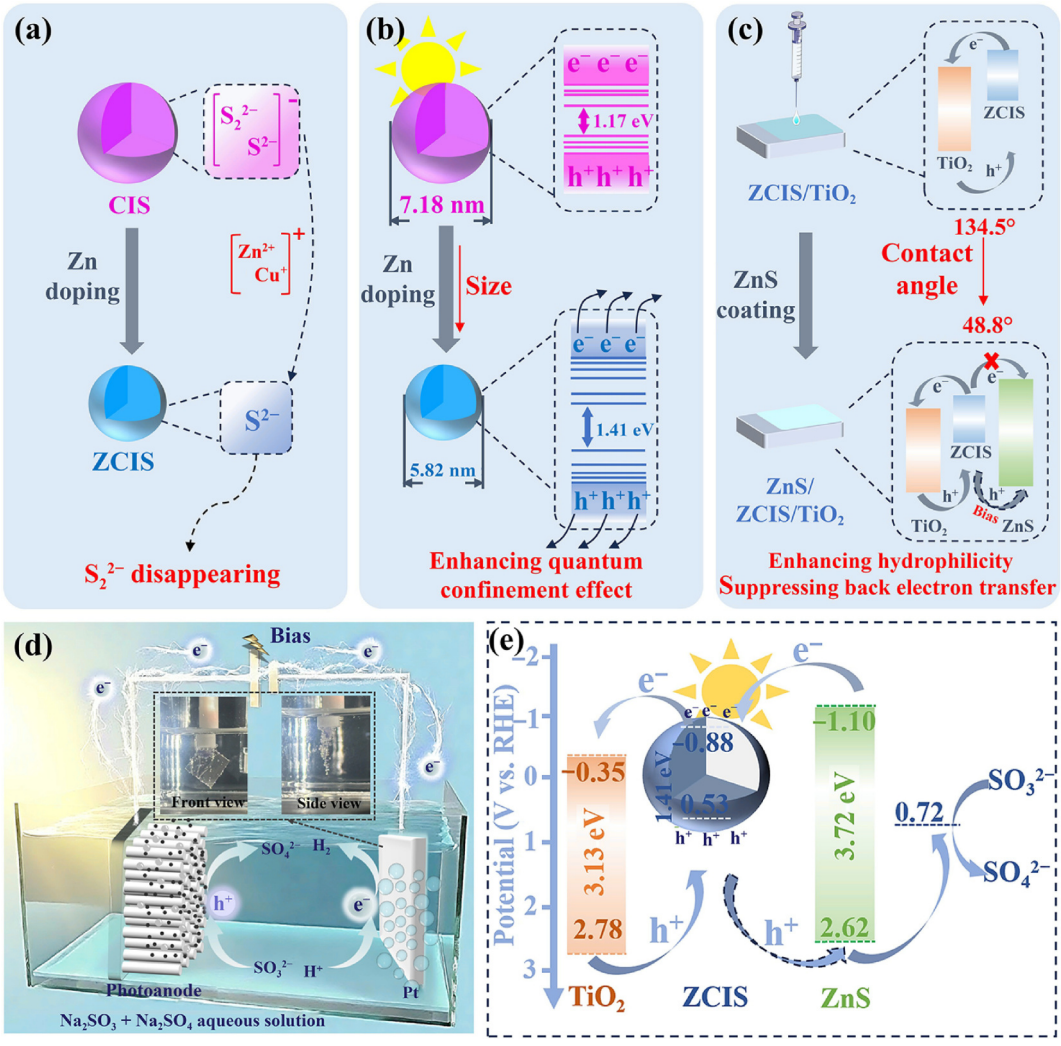

Figure 8 (a) Schematic for H_2 yield and stability improving mechanism caused from the disappearance of S_2^{2-}. (b) Stronger quantum confinement effect. (c) ZnS layer coating. (d) The work principle of ZnS/ZCIS/TiO_2 based PEC cell for H_2 evolution. (e) Energy band alignment and charge transfer in photoanode.

photogenerated electrons in ZCIS QDs inject into CB of TiO_2 and then are collected by the FTO glass, transferring to Pt electrode via the external circuit where they participate in reduction reaction ($2h^+ + 2e^- \rightarrow H_2$). Meanwhile, photogenerated holes in ZCIS inject into VB of ZnS driven by the bias and eventually enrich on the surface of ZnS/ZCIS/TiO_2 photoanode where they oxidize the hole scavenger SO_3^{2-} in the electrolyte ($SO_3^{2-} + 2OH^- + 2h^+ \rightarrow SO_4^{2-} + H_2O$) and are consumed efficiently.

After Zn doping and ZnS coating, the cell constituting ZnS/ZCIS/TiO_2 photoanode and Pt sheet counter electrode achieved hydrogen yield 642.17 μmol/cm² after 4 h with average rate 160.54 μmol/(cm²·h), and the yield maintained 91.5% after 16 h in 0.5 M Na_2SO_3/Na_2SO_4 electrolyte under one sun illumination at 0.6 V bias, which is compared with various sulfide QDs-sensitized PEC cells for hydrogen production reported recently, as shown in Table 1. Although these QDs contain heavy metals (Pb or Cd) or noble metal Ag that are reported high PEC performance as the traditional QDs, ZCIS as non-toxic and low-cost QDs sensitized cells exhibit superior hydrogen production performance and stability. Its excellent hydrogen production performance and stability indicate the great application potential in large-scale and sustainable development of future clean energy systems.

Table 1 The comparison of PEC performance for H_2 evolution of ZnS/ZCIS/TiO_2 photoanode based cell with other reports

QDs photosensitizer	Photocurrent density (mA/cm²)	H_2 evolution rate (μmol/(cm²·h))	Stability of H_2 yield	Reference
$AgIn_5Se_8$	0.125	2.15	—	[36]
$CuCaS_2$	3.5	23	62% after 2 h	[37]
CdS	2.41	24.74	94.1% after 5 h	[38]
PbS	5.56	44.7	91.3% after 10 h	[39]
CuInSe	10.7	50	83% after 4 h	[40]
ZnCuInSe	10.5	52.9	—	[41]
$Cu_xAg_{1-x}InS_2$	5.8	67.4	50% after 2.78 h	[42]
CdS	—	95.4	50% after 35 h	[43]
$Cd_{1-x}Zn_xSe$	13.5	140	99% after 10 h	[44]
Zn:$CuFeS_2$	10.89	160.54	91.5% after 16 h	This work

4 Conclusions

The quaternary Zn-doped $CuFeS_2$ QDs were designed and synthesized with hot-injection method to sensitize the photoanode, and then ZnS was employed as the passivation layer on the

photoanode in solar PEC cell for H_2 evolution. The introduction of Zn ions eliminates S_2^{2-} defects and causes lattice contraction, leading to smaller grain size, and enhancing the quantum confinement effect that accelerates the separation and transfer of photogenerated carriers. ZnS passivation layer in I-type ZnS/ZCIS heterojunction not only suppresses back electron transfer, but also promotes the separation and transfer of carriers furtherly. Under one sun illumination (AM 1.5G, 100 mW/cm^2), ZnS/ZCIS/TiO_2 photoanode based cell has achieved accumulative H_2 yield 642.17 μmol/cm^2 for 4 h with average rate 160.54 μmol/(cm^2·h) at 0.6 V bias. After 16-h H_2 evolution in 4-cycle test, the average decline in evolution rate per cycle was merely 2.13%. The quaternary Zn:$CuFeS_2$ QDs possess higher photochemical stability and more optimizing energy alignment in the photoanode for photogenerated carrier separation, transfer, and transport. ZnS passivation layer promotes the separation and transfer of photogenerated carriers furtherly at an appropriate bias 0.6 V. In a word, these hierarchical regulations provide a way of improving stable applications of sulfide QDs in solar PEC cells.

Electronic Supplementary Material: Supplementary material (the preparation and assembly of PEC cells, the details for characterizations and measurements and DFT calculations, seven tables, eleven figures, and all used equations) is available in the online version of this article at https://doi.org/10.26599/NR.2026.94908672.

Data availability

All data needed to support the conclusions in the paper are presented in the manuscript and the ESM. Additional data related to this paper may be requested from the corresponding author upon request.

Acknowledgements

This work was financially supported by the National Natural Science Foundation of China (No. 52273288), the Natural Science Foundation of Heilongjiang Province of China (No. LH2022E082), and the Natural Science Foundation of Shandong Province of China (No. ZR2022ME215).

Declaration of competing interest

All the contributing authors report no conflict of interests in this work.

Author contribution statement

Y. L.: Data curation, writing manuscript, experimental design. S. S.: Data curation. Y. L. D.: Project administration. Y. N. G.: Project administration. J. W. Y.: Validation. W. Z.: Validation. All the authors have approved the final manuscript.

Use of AI statement

None.

References

[1] Xia, L.; Tong, X.; Yao, Y. S.; Long, Z. H.; Cai, M. K.; Jin, L.; Vomiero, A.; Wang, Z. M. Simultaneous copper incorporation in core/shell-structured eco-friendly quantum dots for high-efficiency photoelectrochemical hydrogen evolution. *Nano Energy* **2024**, *122*, 109302.

[2] García De Arquer, F. P.; Talapin, D. V.; Klimov, V. I.; Arakawa, Y.; Bayer, M.; Sargent, E. H. Semiconductor quantum dots: Technological progress and future challenges. *Science* **2021**, *373*, eaaz8541.

[3] Mi, G. H.; Yao, Y. S.; Xia, L.; Zhao, H. Y.; Yang, Q.; Wang, Z. M. M.; Tong, X. Reinforcing photogenerated carrier extraction of environment-friendly InP/ZnSeS quantum dots for high-performing photoelectrochemical photodetection and solar energy conversion. *Small* **2025**, *21*, 2405275.

[4] Zhang, Y. G.; Wang, Y. H.; Wu, X. L.; Li, T.; Zhao, F. L.; Tan, J. Y.; Liu, M.; Huang, H. W. Photocorrosion of metal sulfides: Mechanism, characterization, anti-photocorrosion strategies and solar catalysis applications. *Coord. Chem. Rev.* **2025**, *545*, 217021.

[5] Li, F. Y.; Zhang, M.; Benetti, D.; Shi, L.; Besteiro, L. V.; Zhang, H.; Liu, J. B.; Selopal, G. S.; Sun, S. H.; Wang, Z. M. et al. "Green", gradient multi-shell $CuInSe_2$/$(CuInSe_xS_{1-x})_5$/$CuInS_2$ quantum dots for photo-electrochemical hydrogen generation. *Appl. Catal. B: Environ.* **2021**, *280*, 119402.

[6] Ji, P. Z.; Li, R.; Xia, X. H.; Zou, J. P.; Chen, X. X. Engineering heterojunction interfacial chemical bonds to adjust electron flow direction for efficient photocatalytic H_2 production. *Appl. Catal. B: Environ. Energy* **2025**, *379*, 125693.

[7] Chen, Y. X.; Zhong, W.; Chen, F.; Wang, P.; Fan, J. J.; Yu, H. G. Photoinduced self-stability mechanism of CdS photocatalyst: The dependence of photocorrosion and H_2-evolution performance. *J. Mater. Sci. Technol.* **2022**, *121*, 19–27.

[8] Kwon, H. G.; Lee, T.; Kim, K.; Kim, D. H.; Seo, H.; Kwon, O. P.; Kwak, J.; Kim, S. W. Enhanced stability and highly bright electroluminescence of AgInZnS/CdS/ZnS quantum dots through complete isolation of core and shell via a CdS interlayer. *Small* **2024**, *20*, 2304592.

[9] Cao, S. Y.; Yan, X. Q.; Kang, Z.; Liang, Q. J.; Liao, X. Q.; Zhang, Y. Band alignment engineering for improved performance and stability of $ZnFe_2O_4$ modified CdS/ZnO nanostructured photoanode for PEC water splitting. *Nano Energy* **2016**, *24*, 25–31.

[10] Hu, Y.; Hao, X. Q.; Cui, Z. W.; Zhou, J.; Chu, S. Q.; Wang, Y.; Zou, Z. G. Enhanced photocarrier separation in conjugated polymer engineered CdS for direct Z-scheme photocatalytic hydrogen evolution. *Appl. Catal. B: Environ.* **2020**, *260*, 118131.

[11] Luo, Y.; Zhang, X. H.; Huang, C.; Han, X. L.; Jiang, Q. Q.; Zhou, T. F.; Yang, H. J.; Hu, J. C. $Zn_{0.8}Cd_{0.2}S$ hollow spheres with a highly dispersed Ni dopant for boosting photocatalytic hydrogen generation. *ACS Omega* **2021**, *6*, 13544–13553.

[12] Nie, L. Z.; Chen, L. Q.; Li, J. Z.; Wang, Y. J.; Wang, X. X.; Zhang, L.; Dong, H. X.; Pan, A. L. Highly efficient Zn:$CuInSe_2$/ZnS quantum dots for near-infrared optical wireless communications. *J. Mater. Chem. C* **2025**, *13*, 7043–7051.

[13] Ge, Q. Y.; Feng, X. Z.; Wang, R. H.; Zheng, R. J.; Luo, S. Y.; Duan, L. L.; Ji, Y. F.; Lin, J.; Chen, H. Mixed redox-couple-involved chalcopyrite phase $CuFeS_2$ quantum dots for highly efficient Cr(VI) removal. *Environ. Sci. Technol.* **2020**, *54*, 8022–8031.

[14] Ntelane, T. S.; Feleni, U.; Mthombeni, N. H.; Kuvarega, A. T. $CuFeS_2$ supported on dendritic mesoporous silica-titania for persulfate-assisted degradation of sulfamethoxazole under visible light. *J. Colloid Interface Sci.* **2024**, *654*, 660–676.

[15] Klauber, C.; Parker, A.; Van Bronswijk, W.; Watling, H. Sulphur speciation of leached chalcopyrite surfaces as determined by X-ray photoelectron spectroscopy. *Int. J. Miner. Process.* **2001**, *62*, 65–94.

[16] Ram, R.; Coyle, V. E.; Bond, A. M.; Chen, M.; Bhargava, S. K.; Jones, L. A. A scanning electrochemical microscopy (SECM) study of the interfacial solution chemistry at polarised chalcopyrite ($CuFeS_2$) and chalcocite (Cu_2S). *Electrochem. Commun.* **2020**, *115*, 106730.

[17] Morrell, C. T.; Davis, V. K.; Dulock, N. V.; Patheria, E. S.; See, K. A. The influence of metal and anion electronic states on the stability of high valent metals. *Coord. Chem. Rev.* **2026**, *547*, 217070.

[18] Liu, C.; Tong, X.; Channa, A. I.; Li, X.; Long, Z. H.; Feng, H. J.; You, Y. M.; Wang, R.; Lin, F.; Dee, C. F. et al. Tuning the composition of heavy metal-free quaternary quantum dots for improved photoelectrochemical performance. *J. Mater. Chem. A* **2021**, *9*, 5825–5832.

[19] Yuan, F. Q.; Ma, S. Y.; Wen, Y. F.; Liu, W. W.; Pei, S. T.; Wang, S. Y.; Zhang, Q. Q.; Shi, J. L. The experimental and theoretical study of Al doped $ZnSn(OH)_6$ to improve gas sensitivity. *J. Alloys Compd.* **2023**, *932*, 167563.

[20] Yuan, F.; Liu, Y.; Ma, P.; Wang, S.; Yang, G. X.; Qin, J. H.; Luo, Y. T.; Luo, S. C.; Ma, J. T. Coupling interface structure in Ni_xS/Cu_5FeS_4 hybrid with enhanced electrocatalytic activity for alkaline hydrogen evolution reaction. *J. Colloid Interface Sci.* **2020**, *578*, 668–676.

[21] Conconi, R.; Del Mar Abad Ortega, M.; Nieto, F.; Buono, P.; Capitani, G. TEM-EDS microanalysis: Comparison between different electron sources, accelerating voltages and detection systems. *Ultramicroscopy* **2025**, *276*, 114201.

[22] Cao, X. Y.; Dong, H. Z.; Zhu, K. J.; Qu, Q. Y.; Jiang, D. J.; Zheng, Y. Z.; Yao, C. P.; Wang, B.; Abdi, F. F.; Luo, W. J. et al. Enhanced performance of quantum-dot-sensitized solar cells by suppressing back transfer in TiO_2/CdS faradaic junction photoelectrode. *Nano Res.* **2025**, *18*, 94907455.

[23] Asor, L.; Liu, J.; Xiang, S. T.; Tessler, N.; Frenkel, A. I.; Banin, U. Zn-doped P-type InAs nanocrystal quantum dots. *Adv. Mater.* **2023**, *35*, 2208332.

[24] Tsuji, M.; Iimura, S.; Kim, J.; Hosono, H. Hole concentration reduction in CuI by Zn substitution and its mechanism: Toward device applications. *ACS Appl. Mater. Interfaces* **2022**, *14*, 33463–33471.

[25] Idris, A. M.; Liu, T. F.; Hussain Shah, J.; Shahid Malik, A.; Zhao, D.; Han, H. X.; Li, C. Correction to "Sr_2NiWO_6 double perovskite oxide as a novel visible-light-responsive water oxidation photocatalyst". *ACS Appl. Mater. Interfaces* **2020**, *12*, 56659–56660.

[26] Gui, X. X.; Zhou, Y. T.; Liang, Q.; Zhou, M.; Li, X. Z.; Xu, S.; Li, Z. Y. Construction of porous ZnS/TiO_2 S-scheme heterostructure derived from MOF-on-MOF with boosting photocatalytic H_2-generation activity. *Int. J. Hydrogen Energy* **2023**, *48*, 38237–38250.

[27] Yi, S. S.; Wulan, B. R.; Yan, J. M.; Jiang, Q. Highly efficient photoelectrochemical water splitting: Surface modification of cobalt-phosphate-loaded Co_3O_4/Fe_2O_3 p–n heterojunction nanorod arrays. *Adv. Funct. Mater.* **2019**, *29*, 1801902.

[28] He, S.; Ghorai, N.; Ashokan, A.; Gebre, S. T.; Yang, Z. C.; Lian, T. Q. *In situ* studies of multi-carrier dynamics in electrochemically-charged colloidal CdSe/CdS core/shell quantum dots. *Angew. Chem., Int. Ed.* **2025**, *137*, e202503972.

[29] Yue, X. Z.; Yi, S. S.; Wang, R. W.; Zhang, Z. T.; Qiu, S. L. Well-controlled $SrTiO_3$@Mo_2C core–shell nanofiber photocatalyst: Boosted photo-generated charge carriers transportation and enhanced catalytic performance for water reduction. *Nano Energy* **2018**, *47*, 463–473.

[30] Yu, L. Q.; Liu, Y. X.; Duan, L. J.; Zhang, Y. P.; Rodrigues, L. A.; Reddy, D. A.; Zhu, H. F. Construction of $SrTiO_3/TiO_2$ heterojunction by *in-situ* ion exchange method to enhance photochemical performance. *Mater. Sci. Eng.: B* **2024**, *299*, 117010.

[31] Xie, H. Y.; Su, X. L.; Zheng, G.; Zhu, T.; Yin, K.; Yan, Y. G.; Uher, C.; Kanatzidis, M. G.; Tang, X. F. The role of Zn in chalcopyrite $CuFeS_2$: Enhanced thermoelectric properties of $Cu_{1-x}Zn_xFeS_2$ with *in situ* nanoprecipitates. *Adv. Energy Mater.* **2017**, *7*, 1601299.

[32] Ye, J. Z.; Gaur, D.; Mi, C. J.; Chen, Z. J.; Fernández, I. L.; Zhao, H. T.; Dong, Y. T.; Polavarapu, L.; Hoye, R. L. Z. Strongly-confined colloidal lead-halide perovskite quantum dots: From synthesis to applications. *Chem. Soc. Rev.* **2024**, *53*, 8095–8122.

[33] Liu, Q.; Cao, F. R.; Wu, F. L.; Chen, S. M.; Xiong, J.; Li, L. Partial ion exchange derived 2D Cu–Zn–In–S nanosheets as sensitizers of 1D TiO_2 nanorods for boosting solar water splitting. *ACS Appl. Mater. Interfaces* **2016**, *8*, 26235–26243.

[34] Wu, N. T.; Liu, X. Y.; Zeng, M.; Gao, J. W.; Lu, X. B.; Zeng, Z.; Zheng, Y. H. Controllable synthesis of novel luminescent $CuFeS_2$ quantum dots with magnetic properties and cation sensing features. *J. Nanopart. Res.* **2019**, *21*, 268.

[35] Gabka, G.; Bujak, P.; Ostrowski, A.; Tomaszewski, W.; Lisowski, W.; Sobczak, J. W.; Pron, A. Cu–Fe–S nanocrystals exhibiting tunable localized surface plasmon resonance in the visible to NIR spectral ranges. *Inorg. Chem.* **2016**, *55*, 6660–6669.

[36] Velásquez, D. A. P.; Sousa, F. L. N.; Soares, T. A. S.; Caires, A. J.; Freitas, D. V.; Navarro, M.; Machado, G. Boosting the performance of TiO_2 nanotubes with ecofriendly $AgIn_5Se_8$ quantum dots for photoelectrochemical hydrogen generation. *J. Power Sources* **2021**, *506*, 230165.

[37] You, Y. M.; Tong, X.; Channa, A. I.; Li, X.; Liu, C.; Ye, H.; Wang, Z. M. Tailoring the optoelectronic properties of eco-friendly $CuGaS_2$/ZnSe core/shell quantum dots for boosted photoelectrochemical solar hydrogen production. *Ecomat* **2022**, *4*, e12206.

[38] Yu, J. D.; Gong, C.; Wu, Z.; Wu, Y. N.; Xiao, W.; Su, Y. F.; Sun, L.; Lin, C. J. Efficient visible light-induced photoelectrocatalytic hydrogen production using CdS sensitized TiO_2 nanorods on TiO_2 nanotube arrays. *J. Mater. Chem. A* **2015**, *3*, 22218–22226.

[39] Ranga, M.; Sinha, S. Photoelectrochemical integrated treatment of textile wastewater by prepared optimized Ni-doped PbS quantum dots on $WO_3/BiVO_4$ along with H_2 production. *Sep. Purif. Technol.* **2025**, *352*, 127928.

[40] Li, S.; Jung, S. M.; Chung, W.; Seo, J. W.; Kim, H.; Park, S. I.; Lee, H. C.; Han, J. S.; Ha, S. B.; Kim, I. Y. et al. Defect engineering of ternary Cu–In–Se quantum dots for boosting photoelectrochemical hydrogen generation. *Carbon Energy* **2023**, *5*, e384.

[41] Li, W. L.; Geng, H. C.; Yao, L.; Cao, K. S.; Sheng, P. T.; Cai, Q. Y. Photoelectrocatalytic hydrogen generation enabled by CdS passivated ZnCuInSe quantum dot-sensitized TiO_2 decorated with Ag nanoparticles. *Nanomaterials* **2019**, *9*, 393.

[42] Guo, H.; Yang, P.; Hu, J.; Jiang, A. Q.; Chen, H. Y.; Niu, X. B.; Zhou, Y. Band structure engineering and defect passivation of $Cu_xAg_{1-x}InS_2$/ZnS quantum dots to enhance photoelectrochemical hydrogen evolution. *ACS Omega* **2022**, *7*, 9642–9651.

[43] Lei, Y. G.; Yang, C.; Hou, J. H.; Wang, F.; Min, S. X.; Ma, X. H.; Jin, Z. L.; Xu, J.; Lu, G. X.; Huang, K. W. Strongly coupled CdS/graphene quantum dots nanohybrids for highly efficient photocatalytic hydrogen evolution: Unraveling the essential roles of graphene quantum dots. *Appl. Catal. B: Environ.* **2017**, *216*, 59–69.

[44] Liu, G. J.; Wang, X. H.; Liu, B. X.; Han, G. T.; Jiang, W.; Zhang, Y. M.; Zhao, H. G. Band engineering enables highly efficient and stable photoelectrochemical hydrogen evolution. *Chem. Eng. J.* **2022**, *450*, 137813.